Assessment of microstructure of alloy Inconel 686 dissimilar weld claddings

CrossMark

Cleiton C. Silva [a, *], Conrado R.M. Afonso [b], Antonio J. Ramirez [c], Marcelo F. Motta [a], Hélio C. Miranda [a], Jesualdo P. Farias [a]

[a] Universidade Federal do Ceará, Departamento de Engenharia Metalúrgica e de Materiais, Laboratório de Engenharia de Soldagem, Campus do Pici, Bloco 715, Fortaleza, Ceará, Brazil
[b] Universidade Federal de São Carlos, Departamento de Engenharia de Materiais, Rodovia Washington Luis, km 235, São Carlos, São Paulo, Brazil
[c] The Ohio State University, Department of Materials Science and Engineering, 1248 Arthur E. Adams Drive, Columbus, OH 43221, USA

ARTICLE INFO

ABSTRACT

Weld overlay with Ni-based superalloys is an important option for industrial applications. New alloys have been developed to assure desirable characteristics such as corrosion resistance. The Inconel 686 superalloy was developed with a higher Cr and Mo content in order to improve its resistance to corrosion. However, information in the literature about the solidification and weld microstructure of this alloy is very limited. This work, which presents important results concerning the microstructure of the Inconel 686 superalloy, focuses on a detailed analysis of the secondary phases formed during solidification using transmission electron microscopy. The results show that there are several Mo-rich precipitates of the P-phase type in the matrix, and the σ-phase and μ-phase in minor amounts.

© 2016 Elsevier B.V. All rights reserved.

1. Introduction

Nickel-based alloys are one of the most corrosion resistant materials used in engineering for a wide range of environments, including high temperatures [1]. Among the many important features of this class of material is its ability to form continuous passive films that protect the material against harsh environments [2]. Hence, these corrosion-resistant alloys have been used as internal and/or external linings of pipelines and offshore production equipment as well as weld claddings on petroleum refining equipment that is associated with corrosive environments [3–5].

Nickel is the main component in these alloys due to its ability to dissolve significant amounts of other alloy elements by maintaining them in solid solution. This allows possibilities for the development of new alloys with specific characteristics and applications [6]. Alloying elements such as Cr, Mo and W are examples of elements that introduce their own special properties to improve corrosion resistance. Cr and Mo are by far the most important alloying elements related to increased corrosion resistance. Together they appear to have a synergistic effect, particularly with regard to localized corrosion [7].

Among the numerous representatives of the Ni–Cr–Mo family hardened by solid solution, the Inconel 625 and Hastelloy C276 alloys occupy a prominent position because they are extensively used in the oil and gas, nuclear and energy industries. The alloy Inconel 625 (UNS N06625), the first generation of Ni-based alloys, was initially developed in 1964 for high temperature operations. However, on the discovery of its excellent corrosion resistance to a variety of corrosive environments, it became important in several different industries [8]. This behavior is mainly due to the high content of Cr (20%) and Mo (9%).

The alloy Inconel 625 has been widely studied in various welding applications (Joining and overlaying) [9–14]. Dupont [3] investigated the characteristics of alloy Inconel 625 welding cladding deposited on 2¼ Cr–1Mo steel and found that the microsegregation of elements such as Fe, Cr, Ni, Mo and Nb were responsible for the solidification of the weld metal. Banovic et al.

* Corresponding author.
E-mail addresses: cleiton@metalmat.ufc.br (C.C. Silva), conrado@ufscar.br (C.R.M. Afonso), ramirezlondono.1@osu.edu (A.J. Ramirez), marcelof@ufc.br (M.F. Motta), hmiranda@ufc.br (H.C. Miranda), jpf@secrel.com.br (J.P. Farias).

[15] studied the use of alloy Inconel 625 for joining parts made of super austenitic stainless steels and found that dilution affects the nickel solubility for elements such as Mo and Nb. Also these authors concluded that minimizing the dilution contributes to maintaining the resistance to corrosion by increasing the nominal concentration of Mo within the alloy.

Hastelloy C276 (UNS N10276) is a second generation nickel-based superalloy, which was developed in 1966. The chemical composition of this alloy has high concentrations of Cr (16% wt.) and Mo (16% wt.), and with the addition of 3–4% wt. W has been successfully applied in many industries due to its good resistance to corrosion in environments containing HCl or chloride ions (Cl$^-$) [16–19]. Although there are several publications in the literature regarding weld joining with this alloy type, little information has been found about weld overlaying with Hastelloy C276 [20–22].

Another member of the Ni–Cr–Mo family is alloy Inconel 686 (UNS N06686/W.Nr. 2.4606), which was developed in 1992 and is a representative of the third generation Ni-based alloys. The alloy Inconel 686 has a Cr content similar to that of Inconel 625 (20% wt.) and Mo content similar to that of Hastelloy C276 (16% wt.) plus 4% wt. W. Its high chromium (Cr) content offers good resistance to oxidizing agents [23]. The high molybdenum (Mo) content provides good corrosion resistance in reducing environments and contributes significantly to increasing resistance to pitting and crevice corrosion in chloride containing environments [23]. The addition of tungsten (W) assists in the formation of the passivating layer, contributing particularly to increase resistance to localized corrosion. The iron and carbon content of the alloy Inconel 686 are limited to low levels to maintain the corrosion resistance properties and to minimize precipitation at grain boundaries, avoiding intergranular corrosion problems, especially in welded components [24].

According to the manufacturer, these features are achieved not only in annealed conditions, but also in similar and dissimilar welding with other Ni-based alloys. Thornton and Cooper [25] tested the alloy Inconel 686 in the welding of super austenitic stainless steel, super duplex stainless steel and other Ni-based superalloys (Inconel 622 and Hastelloy C276) and found superior performance in terms of corrosion with the use of the alloy Inconel 686 as filler metal when compared to the respective weld metals (similar filler metals).

Although the corrosion resistance properties of alloy Inconel 686 are shown in the manufacturers' catalogs and some papers in the literature [25,26], there is little mention of the microstructure in the deposited weld metal in the literature. Furthermore, no information on the metallurgical characteristics of the alloy Inconel 686 used as a corrosion resistant alloy for low carbon, C–Mn and low alloy steels was found. Recently, Maltin and co-workers [27] evaluated the microstructure of welds deposited with the alloy Inconel 686 and observed the presence of incoherent precipitates, whose morphology was considered to be dependent on the concentration of tungsten and dilution.

In addition, Maltin and co-workers concluded that the presence of such phases was detrimental to weld toughness [27]. Investigations on the microstructure of other Ni–Cr–Mo–W superalloys such as alloys 22 (UNS N06022) and Hastelloy C276 (UNS N10276) have shown that there is a segregation of elements such as Mo and W to the interdendritic regions [16,28]. Also the formation of topologically closely packed phases such as P, μ and σ has been reported. These phases can be extremely detrimental to the mechanical properties and corrosion resistance [29,30].

However, information about dissimilar welding between carbon steels and superalloys for mechanical construction are scarce and more studies are needed to assess, for example, the microstructural characteristics, since many of these are susceptible to precipitation

of secondary phases [31–33], solidification cracks [15,34] or other problems that may affect their properties, especially corrosion resistance [35,36].

Thus, systematic studies focused on the development and optimization of welding processes for overlaying applications as well as studies to evaluate the metallurgical compatibility and performance of the deposited weld claddings are of great importance. The aim of this study is to investigate the microstructural characteristics of dissimilar weld overlays of the nickel-based alloy Inconel 686, deposited by the GTAW cold wire feed process, on C–Mn steel substrates.

2. Experimental procedure

The filler metal used in this study was the AWS ER NiCrMo-14 (similar to Inconel 686), and its chemical composition is shown in Table 1. This alloy was chosen as it has special characteristics in terms of high corrosion resistance due to its chemical composition that combines the high Cr content of alloy Inconel 625 with the high Mo content of the alloy Hastelloy C276, and still maintains a low Fe content. These latter two alloys Inconel 625 and Hastelloy C276 are commonly used in the oil industry. The base metal used was the ASTM A516 Gr 60, and its chemical composition is shown in Table 1. This steel was chosen because it is used in the construction of boilers and pressure vessels for the petrochemical and oil & gas industries. Argon with 30% helium was used as the shielding gas.

The welds were performed using an electronic power supply and a data acquisition system to acquire and monitor the values of the current and the tension during the welding. The torch movements were carried out on a robotic workbench, which was important to control the welding speed and to produce the weaving movement (arc oscillation) during the tests. An automatic GTAW wire feeder was used to provide the filler metal. A positioning unit that allowed geometry adjustments was used to guide the wire into the arc weld. Multiple pass welds were applied side-by-side in order to produce the weld cladding. All welds were carried out in the flat position on steel plates of 200 mm × 150 mm × 12.5 mm.

The conditions evaluated were selected from an experiment matrix of the Taguchi method conducted according to previous results. In these studies, we observed that some variables, such as current, welding speed, heat input and weaving (arc oscillation), significantly influenced the geometry and the dilution characteristics of the welds [37,38], requiring more detailed assessment with reference to the effect of the multipass welding on itself.

The welding heat input is determined according to the Eq. [1], where HI is the heat input; I is the RMS welding current; U is the RMS voltage; S is the welding speed and ηis the efficiency. As commented before, one fixed welding current level was used and the different heat inputs were obtained by varying the welding speed. The main parameters selected for the aforementioned welding are shown in Table 2. During the welding, a calibrated data acquisition system was used to measure and monitor the values of the current and the voltage. The welding speed was controlled by a robotic work bench while a calibrated system to measure the wire feed speed was used to assure the correct adjustment of this parameter. An arc efficiency of 0.65 was assumed.

$$HI = \frac{I \cdot U}{S} \times \eta \tag{1}$$

The wire feed speed was proportional to the level of the welding current and therefore was not selected as an independent variable. Furthermore, the best condition to reduce the dilution was achieved when the maximum feed rate was applied for each arc power level [39]. Other variables that had a moderate effect or whose

Table 1
Chemical composition of the filler metal AWS ER NiCrMo-14 and base metal ASTM A516 Gr.60 steel.

Alloy	Chemical composition (%.wt)							
AWS ERNiCrMo-14 (Inconel 686®)	**Ni**	**C**	**Cr**	**Mo**	**W**	**Fe**	**Al**	**Ti**
	58.2	0.01	20.5	16.4	4.0	0.3	0.3	0.04
	Nb	**Mn**	**Si**	**Cu**	**Co**	**V**	**P**	**S**
	–	0.2	0.06	0.01	–	–	0.002	0.001
ASTM A516 Gr. 60	**Ni**	**C**	**Cr**	**Mo**	**Fe**	**Al**	**Mn**	**Si**
	0.01	0.15	0.02	0.01	Bal.	0.02	0.95	0.2

Table 2
Welding parameters.

Test	Current (A)	Welding speed (cm/min)	Voltage (V)	Heat input (kJ/cm)	Wire feed speed (m/min)
A	335	25	24	12	8.5
B		21	23	14	8.5
C		17	20	15	8.0

previous results indicated optimum values for the application of overlays were kept fixed in this study. The electrode tip-to-workpiece distance from (ETWD) was 10 mm.

Although this ETWD value is uncommon for conventional TIG welding in the case of a weld overlay, a previous study [40] showed that the optimum value is related to the lowest possible melting of the base metal without compromising the coalescence between the weld metal and the substrate. The Distance from Tip of the Wire to the Workpiece (DTWW) was set at 3 mm, which presents a good relationship between geometry and dilution [41]. To produce the cladding layer, some weld beads were deposited side by side, overlaying 1/3 of the width of the previous weld bead.

Some minor parameters were maintained constant for all conditions such as: electrode tip (50°), angle of attack of wire feeder guide (50°) and shielding gas flow (15 l/min). The wire feed speed was adjusted to maximum value for each of the conditions, which contributes to a low dilution level. Additional details concerning the adjustment of the geometry in the wire feeder guide and the feed rate are described by Miranda et al. [41].

After the welding, the dilution of the claddings was measured in two ways: one based on a metallographic method in which the cross-sectional area of the weld metal was evaluated and the second through the chemical composition. Samples of the test plates were cut for macro and micro analyses. These samples were conventionally prepared for the metallographic evaluation; that is they were ground with silicon carbide waterproof sandpaper and polished using diamond past to a final 1 μm mash, and subsequently chemically etched with a 2 pct Nital solution for the ASTM A516 Gr.60 steel and electrolytically etched using 10%wt. chromic acid solution applying 2 V for 15–20 s (Fig. 1). These samples were used for both analyses: dilution and microstructural characterization.

Image analysis software was used to determine the cross-sectional area of the weld overlay. In this cross-section the area added by the deposition of the filler metal (nickel alloy) (A_{fm}) and the area corresponding to the base metal (steel) melted during the welding (A_{bm}) were measured. Thus, dilution corresponded to the ratio between the melted steel area and total area of the weld overlay, which is the sum of both areas ($A_{fm} + A_{bm}$), according to Eq. [2]. The second method involved determining the chemical composition using energy dispersive X-ray spectroscopy (EDS). Based on the results of the iron content in the weld metal the dilution was calculated using Eq. [3], where D is the dilution, and Fe_{wm}, Fe_{fm}, and Fe_{bm} are the iron contents in wt pct of the weld metal, the filler metal and the base metal, respectively.
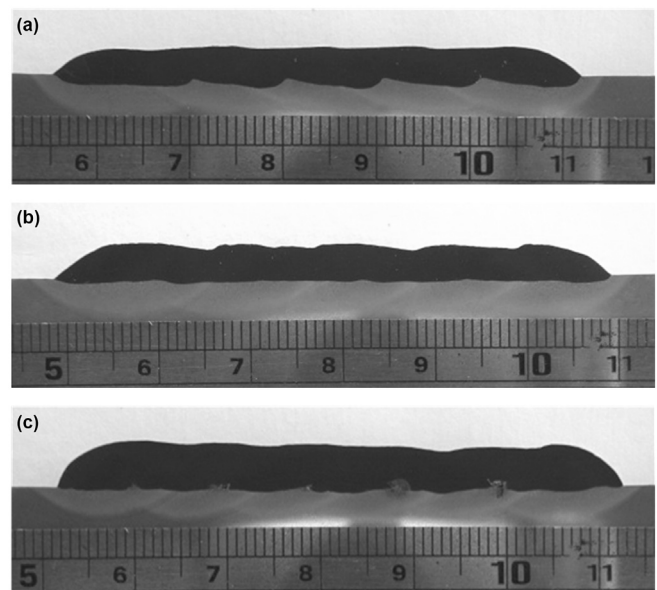

Fig. 1. Cross-section macro structure of the claddings deposited with 686 alloy. (a) Sample A; (b) Sample B; (c) Sample C.

$$D = \frac{A_{bm}}{\left(A_{fm} + A_{bm}\right)} \times 100 \qquad (2)$$

$$D = \frac{Fe_{wm} - Fe_{fm}}{Fe_{bm} + Fe_{fm}} \times 100 \qquad (3)$$

The microstructures were examined by two scanning electron microscopes (SEM), models Phillips XL30 and Carl Zeiss EVO 40, using the Everhart-Thornley detector to produce secondary electron (SE) images. Both SEM were equipped with energy dispersive X-ray spectroscopy (EDS) systems. Samples for characterization were examined by transmission electron microscopy (TEM) and scanning transmission electron microscopy (STEM), operating in both bright-field and dark-field modes. The samples were extracted and prepared in the plain view section. The TEM/STEM analyses were performed using a JEOL JEM 2100 ARP microscope coupled to an EDS microanalysis system.

X-ray diffraction analysis (XRD) was also used to characterize

the secondary phases precipitated during solidification and/or solid state transformation. This evaluation was carried out according the ASTM 936 standard which covers the procedures for the isolation of TCP (topologically close-packed) in nickel-based alloys. The Panalytical XPert Pro MPD X-ray spectrometer was used in the present investigation. For post-processing and peak matching the X'Pert HighScore software and its database were used. The scan details applied in these analyses were: 2Theta range from 30 to 90 deg. with a step size of approximately 0.02 deg. and counting at each step for 4 s. Cu Ka radiation was used and the X-ray generator power was set at 40 kV and 40 mA.

3. Results and discussion

3.1. Dilution and macroscopic evaluation

The macrostructure of the claddings is shown in Fig. 1. On evaluating the weld zone macroscopically some defects along the interface of Sample C were found (Fig. 2). This was assumed to be the result of cold lap during the overlap. No cracks and other types of macroscopic defects such as pore or bubble gas were observed for all tested conditions. An exception which is presented in Fig. 3a were small spherical cavities decorated with a secondary phase net. A detail of this net of secondary phases rich in Mo is shown in Fig. 3b. The most accepted hypothesis to justify the formation of this structure was attributed to the inclusion of Al/Mg oxides formed during solidification. The EDS analysis was performed on the region indicated by the arrow in Fig. 3b. The result indicated a high concentration of oxygen, aluminum and magnesium, which are commonly added as deoxidizing agents and are strong formers of oxide inclusion. Thus, it is possible that these inclusions form the spherical cavities, and are dissolved during etching to reveal the microstructure.

The different welding conditions used in this study resulted in different levels of dilution, as can be seen in Fig. 1. The data presented in Table 3 shows that the condition with lowest heat input had the highest dilution, while the condition with the highest heat input resulted in the lowest dilution. This behavior was attributed to the barrier effect: the reduced welding speed caused a liquid metal accumulation which increased the volume of the weld pool. This bulkier weld pool acts as a barrier to the arc on the substrate. Thus, less heat is transferred directly to the steel and hence less fusion of the substrate occurs.

The results of the chemical composition of the weld claddings measured on the cross-section in low magnification ($80\times$) by energy dispersive X-ray spectroscopy (EDS) are shown in Table 3. This Table gives the main chemical elements of the alloys in question, as well as any secondary elements, present in small amounts. The results of the Fe evaluation show that this element ranged from 6.0 wt% to 19.5 wt%, which indicates there is a large variation in dilution, as will be shown later.

The Cr content ranged from 19.8 to 16.9 wt%, which in two of the three conditions tested were very close to that established for the pure alloy without dilution which is 20 wt% ± 2.0. The Mo content ranged from 14.2 wt% for sample A, whose Fe content was 19.5 wt%, up to 16.2 wt% for sample C with a Fe content of 6.0 wt%. The tungsten (W) content was 4.3 wt% for the highest sample dilution, while there was an increase observed for all other samples that were about 4.8 wt%. Some secondary elements, such as Mn and Si in very low quantities, were also observed, and the carbon content was estimated based on dilution.

3.2. Microsegregation

This section details the microstructural features observed during the analysis of the alloy Inconel 686 applied in this study. Few studies on this alloy were found in the literature, and of these, almost none gave any details of the microstructure; only reviewing their corrosion resistance properties. Thus, this work gave greater emphasis to the microstructure of this alloy in order to contribute to a better understanding of the metallurgical aspects, and thus contribute to the scientific and technological knowledge of the Ni–Cr–Mo–W class of welding alloys.

The as-welded microstructure of the alloy Inconel 686 claddings was made up of a γ-fcc matrix with precipitated secondary phases in the intercellular and interdendritic regions. Fig. 4 shows the chemical composition profile transversely to the direction of cellular growth, which has an increase in molybdenum in the intercellular region, and for the same region there is a depletion of Ni. This Figure also showed a trend to segregate W to the interdendritic region. Quantitative analyses of the chemical composition of the dendrite core were done by measuring five points in each region and the average is presented in Table 4. The results indicated a significant difference in concentration of the alloying elements, especially Ni and Mo.

The different chemical compositions of the dendrite core (Cs) and the global chemical composition (C_0), which correspond to the concentration of the first solid to be formed (Cs) during solidification are shown in Table 3. In addition, the concentration of the liquid at this time was assumed to be the nominal concentration of the alloy (C_0). These differences demonstrate the importance of determining the segregation coefficient k, according to Eq. [4], which is derived from the Scheil equation. In this work a modeling of solute redistribution where there is negligible solid diffusivity
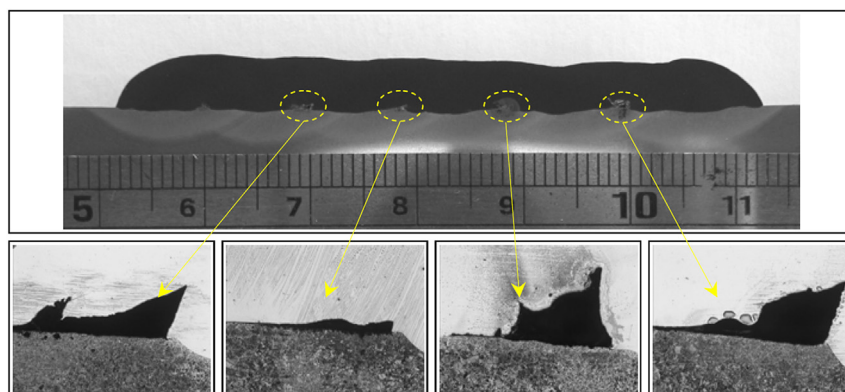

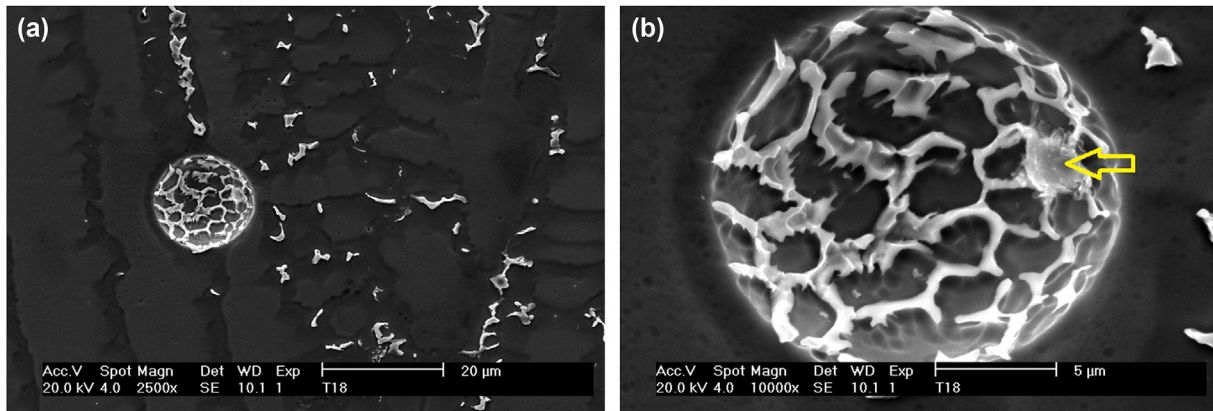**Fig. 2.** Cross-section of Sample C showing the weld zone macroscopically and some defects along the interface.

Fig. 3. (a) Spherical cavities decorated with a secondary phase net. (b) A detail of this cavity and net of secondary phases rich in Mo.

Table 3
Dilution results measured by metallography and composition as well as the concentration of chemical elements of the samples assessed.

Samples	Dilution (%)		Chemical composition (% wt.)							
	Metallography	Compositional	Ni	Cr	Mo	Fe	W	Mn	Si	C*
A	22.0	19.5	44.8	16.9	14.2	19.5	4.3	0.3	0.2	0.043
B	8.7	9.4	50.5	19.1	15.7	9.5	4.8	0.2	0.2	0.020
C	7.0	6.1	52.6	19.8	16.2	6.3	4.8	0.2	0.2	0.018
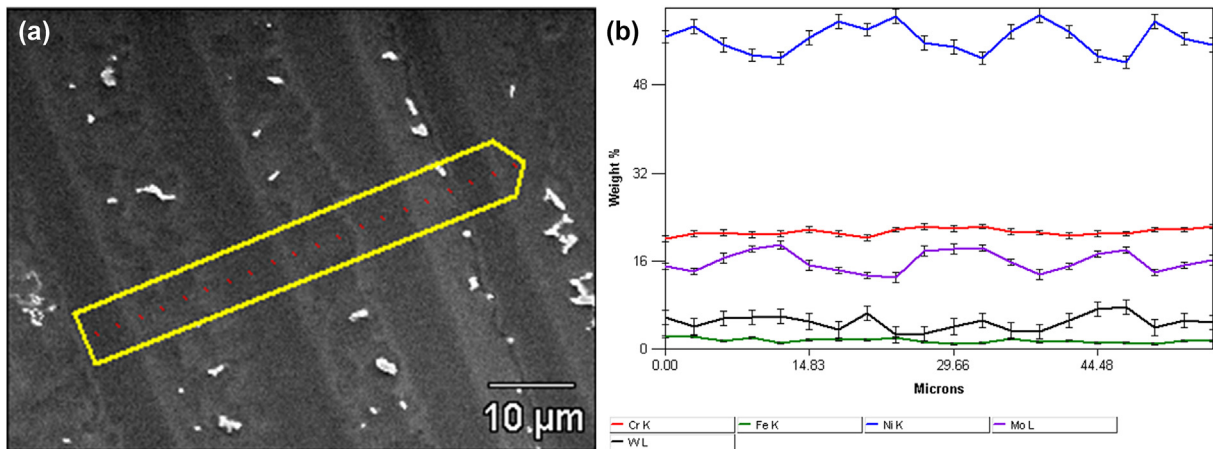
Fig. 4. Chemical composition profile transverse to the cellular-dendritic growth direction obtained by EDS microanalysis: (a) SEM image in SE mode; (b) Elemental distribution along the linescan.

Table 4
Chemical composition at the dendrite/cell core (C_s), nominal concentration (C_0) and segregation coefficient (k).

Element	Sample A			Sample B			Sample C		
	C_s	C_0	K	C_s	C_0	k	C_s	C_0	K
Ni	46.92 ± 0.34	44.81 ± 0.72	1.05	53.93 ± 0.25	50.53 ± 0.18	1.07	55.63 ± 0.36	52.63 ± 0.75	1.06
Cr	16.34 ± 0.23	16.94 ± 0.27	0.96	18.53 ± 0.14	19.03 ± 0.11	0.97	19.41 ± 0.22	19.79 ± 0.23	0.98
Mo	11.05 ± 0.13	14.19 ± 0.60	0.78	12.62 ± 0.10	15.74 ± 0.18	0.80	13.27 ± 0.48	16.20 ± 0.24	0.82
W	4.18 ± 0.24	4.26 ± 0.10	0.98	4.84 ± 0.12	4.77 ± 0.15	1.02	4.99 ± 0.18	4.85 ± 0.13	1.03
Fe	20.96 ± 0.59	19.51 ± 0.82	1.07	9.59 ± 0.29	9.50 ± 0.55	1.01	6.23 ± 0.39	6.03 ± 0.68	1.03

was assumed. This is in agreement with many works found in literature for the alloying additions within nickel based superalloys [3,27]. As commented previously, in this work the concentration of the dendrite core (Cs) at the start of solidification was considered to correspond to the first solid to nucleate, and the concentration of

the liquid at this time was considered to be the nominal concentration of the alloy (C_0), both of which were measured by energy dispersive X-ray spectroscopy (EDS) and the results are shown in Table 3.

$$k = \frac{C_S}{C_L} \tag{4}$$

The segregation coefficient for Ni was k > 1, indicating that this element had been incorporated to form the solid. Molybdenum presented a coefficient k < 1, indicating a strong tendency to segregate to the liquid metal during solidification. The Fe showed partitioning coefficient k > 1. This indicate that the iron is being segregated into the solid. The results of Cr indicate a slight tendency to segregate to the liquid (k < 1), as the "k" values are very close to 1. In fact, the results from the EDS analysis do not show any significant variation of Cr concentration between the dendrite core and the global concentration in the bulk, as can be seen in Fig. 4b. As for W, the results were not conclusive, since they showed values of k very close to 1 and a high dispersion and major std. deviation, the analysis of the k coefficient for W was not statistically significant. Thus, different behavior was found in one sample with a slight tendency to segregate to the liquid (k < 1) and in another to the solid (k > 1).

The results of the segregation coefficient k indicate a strong tendency for Mo to segregate during solidification. The data for Mo are compatible with those found by other authors for Ni-based alloys with the addition of Mo [35,42]. Special attention should be given to the results observed for W, which according to its dilution coefficient segregated to the intercellular/interdendritic region. The variation in the concentration of W and its segregation to the intercellular/interdendritic region is an intriguing fact, since several studies in the literature have reported that W has been added to alloys with high Mo contents exactly in order to enrich the dendrite core, thus minimizing the effects associated to the loss of corrosion resistance due to Mo depletion in the dendrite core [43,44].

Cieslak et al. [16] evaluated the segregation of various elements present in the C4, C22 and C276 alloys, especially W. However, the authors could not identify any segregation patterns for the said element due to the large variation of the results. Dupont et al. [9] investigated the behavior of tungsten microsegregation and according to these authors there was initially a low potential for segregation of this element; but its behavior has not yet been fully understood. However, when Maltin and co-workers [27] analyzed welds, they found a microsegregation coefficient k of less than 1, indicating a tendency for W to segregate to the liquid metal.

3.3. Secondary phase precipitation

3.3.1. Scanning electron microscopy analysis

The different behaviors of the micro segregation of various elements, in particular Mo, during solidification are mainly responsible for the formation of the secondary phases observed in the intercellular regions and the interdendritic solidification grain boundaries. The study on the formation of secondary phases assessed the main morphologies found in the weld metal volume. However, before commenting on the characterization of the secondary phases, a brief comment on the differences between the phases formed in the intercellular regions and interdendritic is required.

Fig. 5 shows two distinct regions in the solidification mode. The first (Fig. 5a) is the area of cell-dendritic growth, in which the formation of secondary phases in the intercellular volume can be seen. The alignment in the region between the cells favored the formation of long strings of the secondary phase. The presence of these elongated chains of precipitates in the intercellular volumes can significantly impair the mechanical properties not only because they are brittle phases, but also due to their orientation, providing a preferential path for crack propagation. As for the columnar dendritic growth (2nd region) the volumes for the formation of secondary phases become narrower due to the growth of secondary arms, which help to break the continuity of the secondary phases, making smaller particles, as can be seen in Fig. 5b.

Please note that cell and cell-dendritic structures are located at the bottom of the fusion zone, just after the interface region. The dendritic zone growth similar to that shown in Fig. 5b comprises most of the weld metal volume. At the top of the fusion zone for the samples with high heat input welding, a coarse dendritic structure with a significant increase in the amount of secondary phases was also observed along all interdendritic boundaries, as shown in Fig. 6a. A detailed evaluation of this region indicated the formation of a special secondary phase, with a morphology characteristic of an eutectic-like structure, as shown in Fig. 6a and b.

The mapping of the chemical composition of these eutectic structures is shown in Fig. 7. The results indicate a depletion of Ni and a significant increase in the concentration of Mo in the secondary phase. No change in the concentration of the other elements such as Cr, W and Fe was detected. In fact, since the alloy Inconel 686 has a high Mo content, which has a strong potential for segregation and is also a strong element for the formation of TCP phases, then the formation of phases like μ, σ and P which are rich in Mo can be expected.

Perricone and DuPont [35] conducted a very interesting study on the solidification of some different Ni–Cr–Mo and Fe–Ni–⊕ Cr–Mo alloys. In one of the Ni-based alloys studied a eutectic constituent was found, very similar to the eutectic phase observed in the present investigation. Those authors also identified this intermetallic phase in the eutectic constituent as an orthorhombic P phase.

A second morphology observed in most samples welded with the alloy Inconel 686 were the precipitates with a lamellar aspect located inside the cell-dendritic growth zone, as shown in Fig. 8. These phases were predominantly found in the region close to the bottom of the melted pool. The SEM micrograph (Fig. 8a) shows the distribution of secondary phases formed in the interdendritic region, and also the direction of growth relative to the direction of solidification can be seen. Fig. 8b provides details of this particular morphology. A striking feature of these phases is the alignment of thin plates in a preferred direction. The direction of growth of the γ-fcc solid during solidification can be determined by aligning the cells/dendrites. Lines drawn parallel to the plates or lamellae of a secondary phase show that they have, in general, an angle of approximately 45° relative to the direction of growth of the cells/dendrites. The weld metal solidifies with a cube texture with a [100] growth direction, and has a 45° [101] crystallographic direction. These features may be indicative of a growth orientation relationship between the plates or lamellae and the γ-fcc matrix, following a [100]γ//[101]TCP direction of growth. Other examples of lamellar particles are shown in Fig. 8c and d, where the same behavior was found.

The chemical analysis of an exemplary precipitated with this lamellar morphology is shown in Fig. 9. The results showed only a slight reduction in nickel content and an increase in the concentration of Mo, indicating that it is a Mo rich TCP phase. However, it should be noted that the chemical analysis by EDS was difficult due to the small size of the secondary phase plates.

This type of morphology is considered to be unusual for TCP phases in solid solution strengthened Ni based alloy weld metals. However, some studies in the literature have pointed out the precipitation of the orthorhombic P-phase in a cell way at high angle grain boundaries in alloys with high levels of Re and W [45,46]. Walston et al. [47] reported that the presence of these P-phase colonies with cellular morphology resulted in a substantial
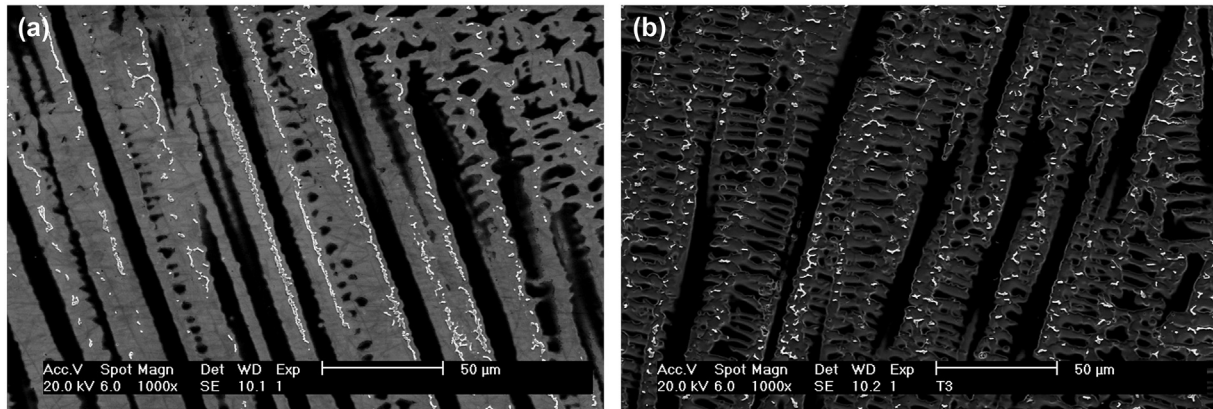
Fig. 5. (a) Formation of secondary phases within intercellular volume. (b) Formation of secondary phases within interdendritic volume.
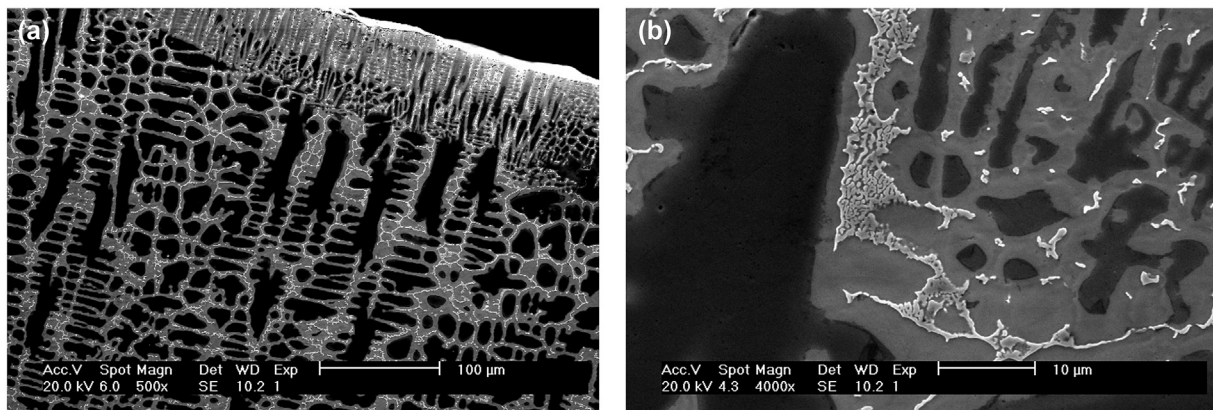

Fig. 6. Top coating microstructure showing the formation of the eutectic morphology.

decrease in the creep strength due to crack propagation along the edges of the cells.

Nystrom et al. [46], who studied the microstructure of Ni alloys hardened by γ' precipitation, observed the formation of a cellular structure formed by three-phase γ, γ' and phase P, the latter being rich in Re. In morphological terms the lamellar structure found in the alloy Inconel 686 claddings and the cellular structure reported by Nystrom et al. [46] present a certain similarity, such as the orientation observed between the lamellae of the secondary phase and the matrix. The present study also found that the P phase plates were often aligned approximately along the [101] crystallographic direction while the array grew along the cube direction [100], as shown in Fig. 10. This reinforces suspicions that the lamellar structure consists of a P phase rich in Mo.

Precipitates with long columns of secondary phases formed along the intercellular and/or interdendritic matrix were also commonly observed. This type of precipitate, together with small blocks along the interdendritic regions were the most common forms of precipitates observed in the microstructure of the alloy Inconel 686 claddings.

Fig. 11 shows the chemical mapping of these elongated phases formed along the intercellular region. As can be seen, the phase has become enriched in Mo and has undergone an impoverishment of Ni and Fe. Cr remains uniform between the matrix and the precipitate, whereas W is scattered without any preferential concentration according to the EDS mapping.

The concentration of elements in the precipitates depends on the overall composition of the alloy. In the Sample C the chemical composition of some elongated precipitates, which had been observed by SEM in the growth cell/dendritic region of the alloy Inconel 686 claddings, were determined by EDS. These analyses indicated a high percentage of molybdenum (36.3 wt%), a Ni content of 22.0 wt%, 18.4 wt% for Cr, and 15.9 wt% for Fe and 7.43 wt% for W. Calculating the values of Ni_{eq}, Cr_{eq} and Mo_{eq} according to Cieslak et al. [16], the precipitate has a Ni_{eq} equal to 37.9 wt%, Mo_{eq} equal to 43.7 wt% and the Cr_{eq} remains at 18.4 wt%. These values are consistent with the ones presented by Raghavan et al. [30].

3.3.2. Transmission electron microscopy analysis

The precipitates present in the bulk weld metal were analyzed by TEM. Fig. 12a gives an example, in the bright field mode, of a precipitate commonly observed in the alloy Inconel 686 weld metal. The structure of the precipitate is uniform, without the presence of stacking faults and/or other crystalline defects. Using the selected area diffraction (SAD) pattern the precipitate was identified as a P phase with an orthorhombic crystal structure, Pbnm space group and lattice parameters: a = 0.907 nm; b = 1.701 nm and c = 0.474 nm (Fig. 12a).

The results of the chemical analysis of the precipitate by EDS (Fig. 12b) are shown in Table 5. The element molybdenum had a high concentration, with an average value of 48.9 wt%. There was also a significant amount of W, with an average of 6.2 wt%, which corresponds to a concentration of almost 50% more than the nominal alloy (4.0 wt%). The concentration of Cr was a little lower than its concentration in the alloy. Considering the values in atomic percentage and using the equations of Ni_{eq} and Mo_{eq}, the values are
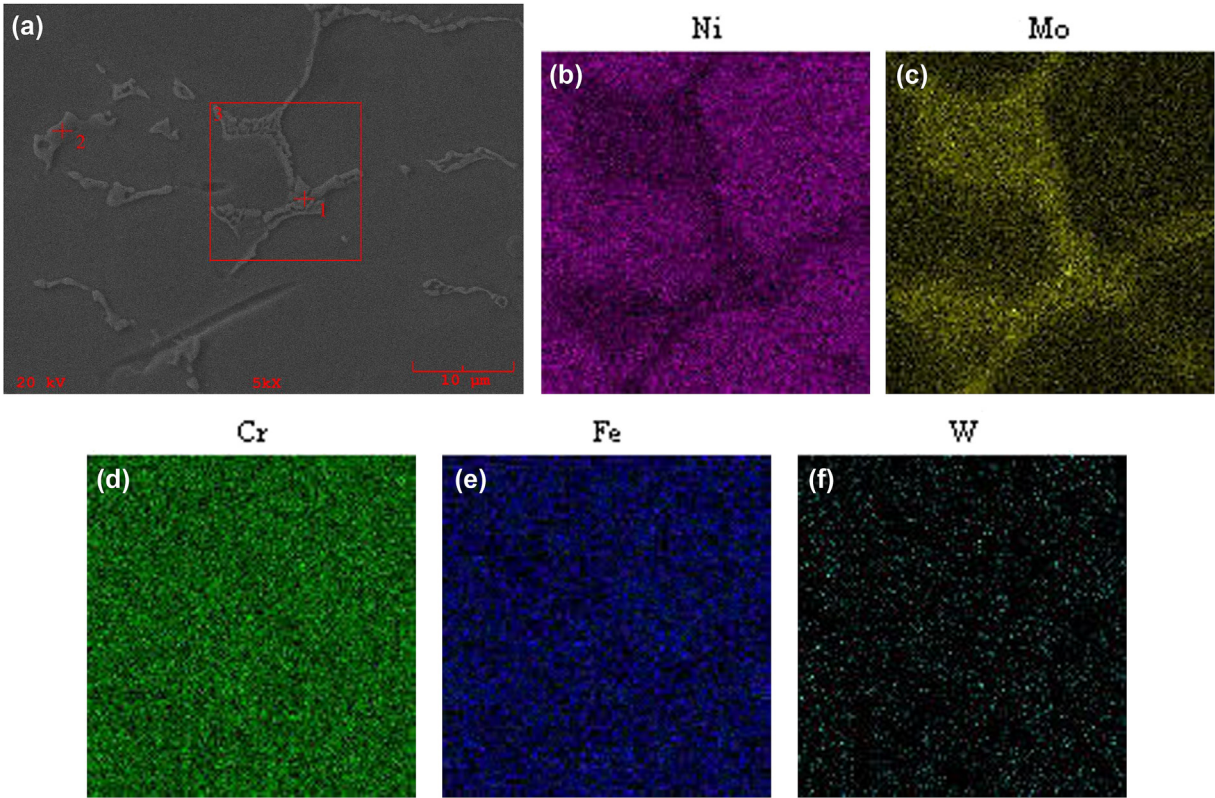
Fig. 7. Elemental mapping of a precipitate with an eutectic morphology. (a) SEM image; (b) Ni; (c) Mo; (d) Cr; (e) Fe; (f) W.
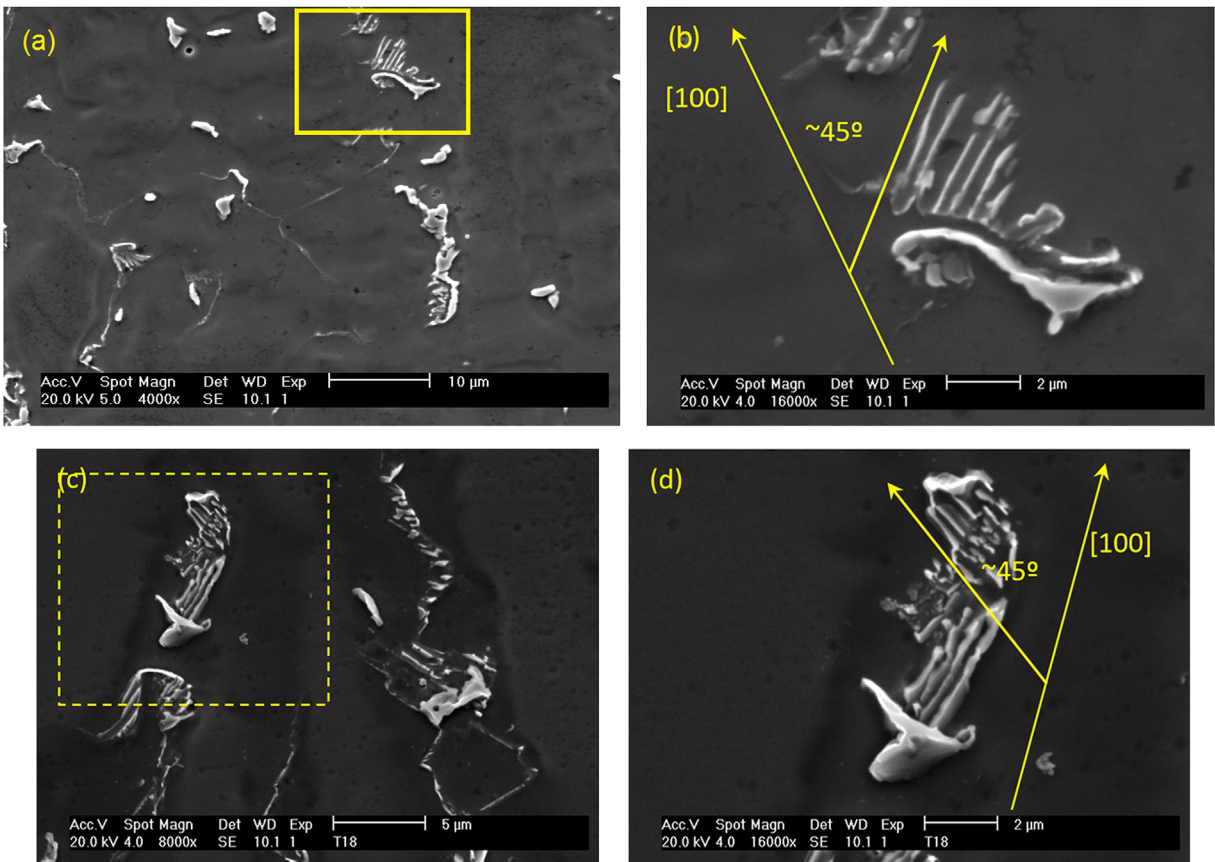

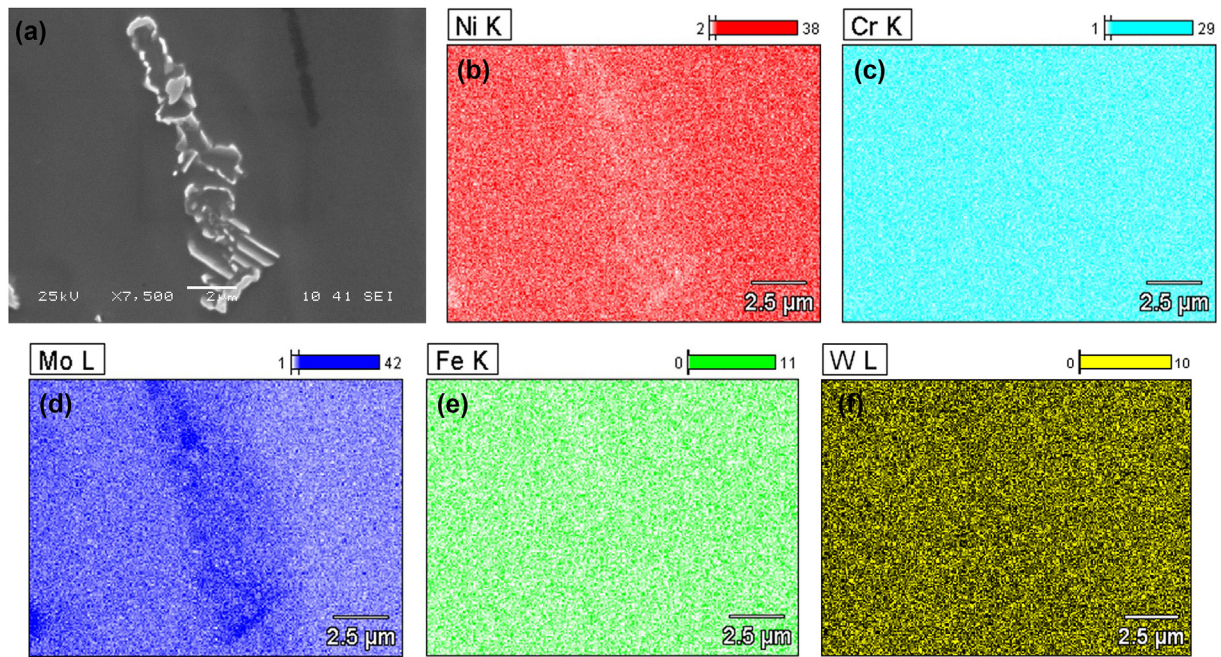**Fig. 8.** Examples of precipitates with lamellar morphology found in Sample C.

Fig. 9. Elemental Mapping of a precipitate with lamellar morphology. (a) SEM image; (b) Ni; (c) Cr; (d) Mo; (e) Fe; (f) W.
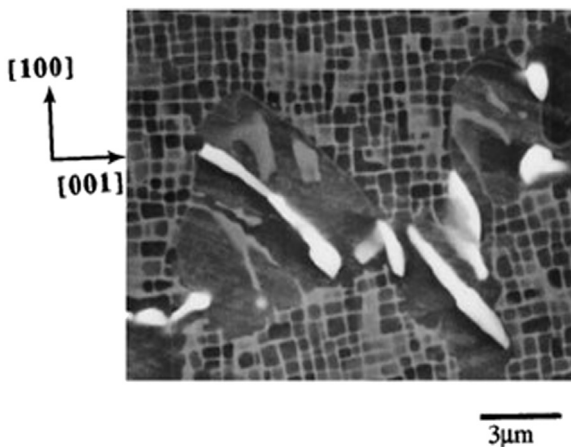

Fig. 10. Precipitation of P-phase cellular morphology rich in Re in a Ni-based alloy strengthened by precipitation [46].

consistent with those expected for the phase P. The chemical composition of the phase P, in general, was similar to that normally observed in other studies. Its chemical formula is written as $Cr_{11.4}Ni_{19}Mo_{20}$, which is consistent with the standard formula for the P-phase, which is $Cr_9Ni_{20}Mo_{21}$.

A second example of a precipitate was observed in the alloy Inconel 686 claddings. The TEM bright field image (Fig. 13a) shows the presence of a precipitate with crystalline structure characteristics of the P-phase and a second precipitate in which many defects are observed in the crystal structure. Fig. 13b shows a detail of the second precipitate, highlighting the defects in the crystal structure.

The first precipitate, whose characteristics are similar to those previously presented, was identified as a P phase, according to its diffraction SAD pattern (Fig. 13a). The selected area diffraction pattern of the second particle observed (Fig. 13a), which has a great number of defects in the crystal structure, identified it as being a μ-phase with a rhombohedral crystal structure, space group R-3m

and lattice parameters: a = b = 0.476 nm and c = 2.562 nm. Indexing of this phase was made considering the data for the μ-phase type Co_7Mo_6.

The defects presented in the μ-phase were characterized as stacking faults. The presence of stacking faults in TCP phases has been reported by other authors [16,30,48]. According to Raghavan et al. [48] stacking faults were observed in the three main types of TCP phases present in Ni–Cr–Mo alloys μ, P and σ. However, these authors pointed out that the P phase and the σ phase have a much lower amount of defects compared to the μ–phase. The authors commented that the high density of stacking faults in the μ–phase is a hallmark of this phase and can be used to distinguish the μ–phase from the remaining phases.

The chemical composition determined by EDS analysis for the μ–phase and P-phase are shown in Table 5. Some differences in chemical composition between the P-phase and the μ–phase were verified. Starting with Cr, there is a lower Cr content of about 11 wt% in μ-phase when compared with nearly 16 wt% in the P-phase. There was no change for Fe. The concentration of Ni in the μ-phase was a little lower than the concentration in the P-phase. The Mo percentage in the μ-phase was about the same as the P-phase. Finally, W presented a more significant change than Mo, increasing its content in the μ-phase by more than 100% when compared with the P phase, increasing from 6.2 wt% to 14.2 wt%.

Although there is little information in the literature on the microstructure of alloy Inconel 686, similar results have been reported in the literature on the solidification of other types of Ni–Cr–Mo–W alloys like the C276 alloy. Cieslak et al. [16] studied the solidification of this alloy and found that the solidification begins with the γ–fcc crystallization at about 1,285 °C and solidification continues with the formation of the P-phase from the liquid, enriched in Mo. Perricone et al. [17] also assessed the solidification path for Hastelloy classes and concluded that the solidification process occurs following the same path shown above. Furthermore, computational thermodynamic analyses have shown that part of the σ phase can also be transformed into a P-phase by a solid state phase transformation process.

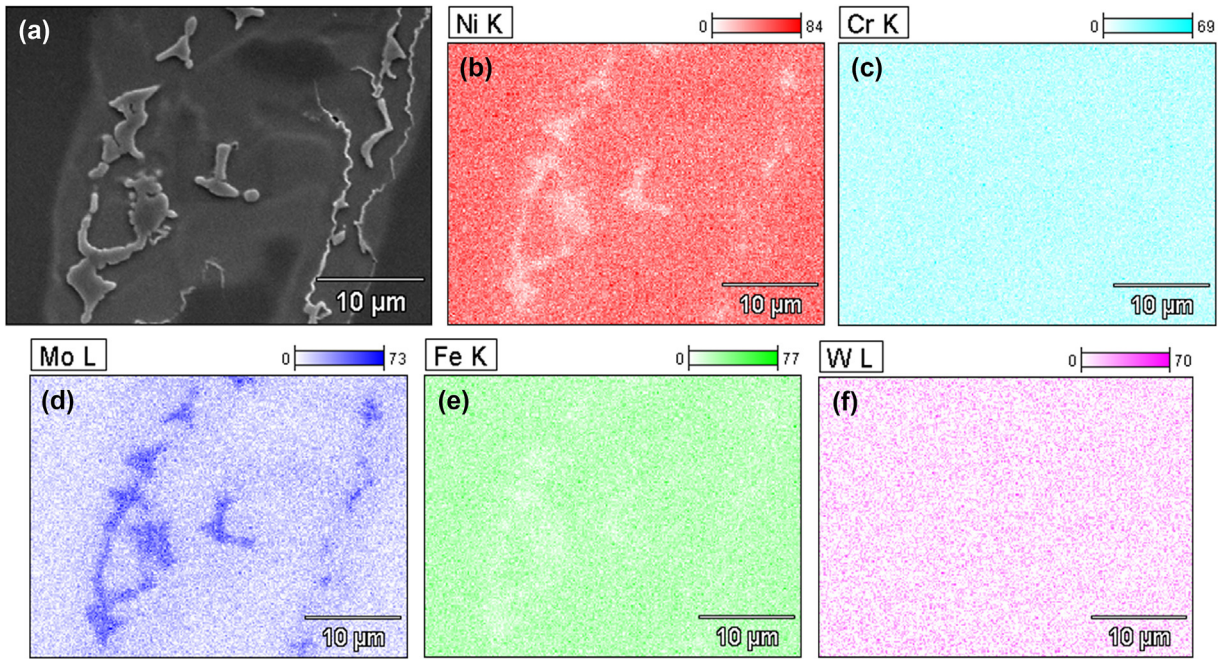Due to the different welding thermal cycles carried out in multi-

Fig. 11. Chemical elemental mapping of a precipitate within the intercellular region. (a) SEM image; (b) Ni; (c) Cr; (d) Mo; (e) Fe; (f) W.
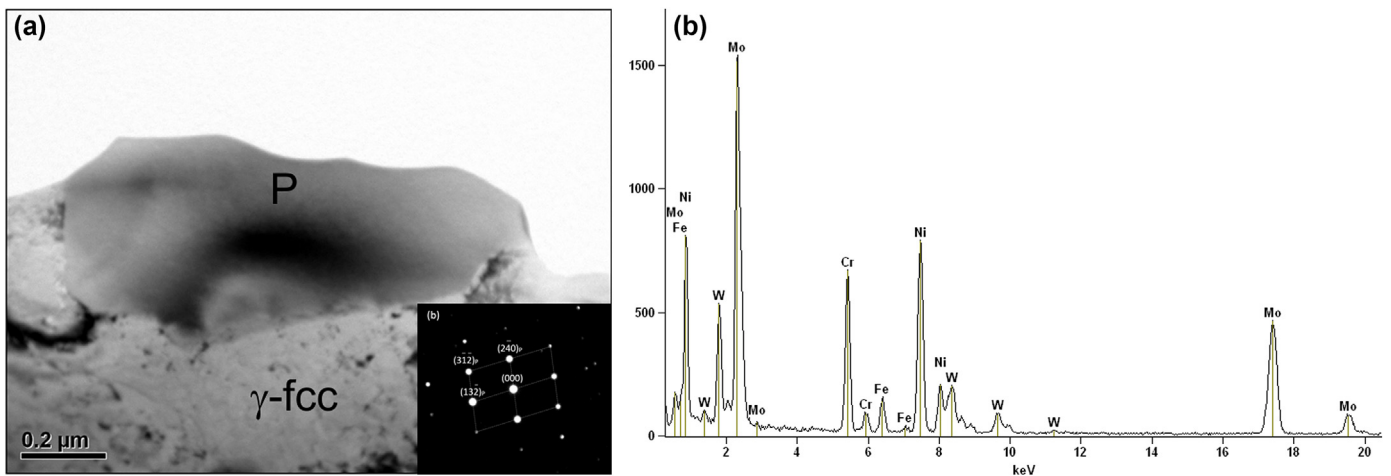

Fig. 12. (a) Transmission electron microscopy image in the bright field showing a P-phase precipitate with selected area diffraction pattern with zone axis oriented according to [425]. (b) Spectrum obtained by EDS analysis.

Table 5
Chemical composition of the main secondary phases observed in the weld metal. Semi-quantitative results performed by EDS.

Chemical composition of the main secondary phases						
Element	μ-phase		P-phase		σ-phase	
	% Weigh	% Atomic	% Weigh	% Atomic	% Weigh	% Atomic
Cr (K)	11.2 ± 0.2	18.7 ± 0.4	15.9 ± 0.3	22.8 ± 0.4	23.4 ± 0.3	30.3 ± 0.3
Fe (K)	3.5 ± 0.2	4.7 ± 0.2	3.8 ± 0.2	5.1 ± 0.2	5.5 ± 0.2	6.6 ± 0.2
Ni (K)	19.8 ± 0.5	30.3 ± 0.4	25.2 ± 0.5	33.0 ± 0.6	34.0 ± 0.5	38.9 ± 0.4
Mo (K)	51.4 ± 1.2	40.6 ± 1.3	48.9 ± 0.9	36.6 ± 0.7	31.7 ± 0.8	22.2 ± 0.5
W (L)	14.2 ± 0.8	6.6 ± 0.4	6.2 ± 0.6	2.5 ± 0.2	5.4 ± 0.9	2.0 ± 0.3

pass welding, other transformations may occur in the solid state after the solidification. Considering the phase diagram for the temperature 850 °C [30], the final solidification region, whose chemical composition corresponds to the P phase precipitates, now lies within the biphasic field γ + μ, resulting in a partial transformation of the P phase into the μ−phase. Since the cooling rates achieved during the welding process are significantly higher, the material remains for a short period of time in the transformation
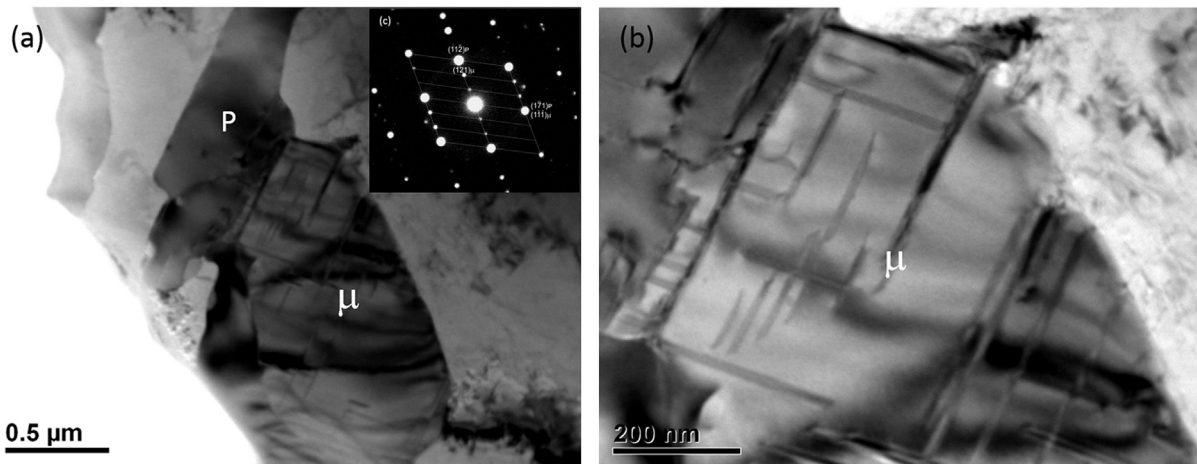
Fig. 13. (a) TEM image in the bright field of an agglomerate formed by P and μ phases with selected area diffraction pattern; (b) In detail the μ-phase structure showing stacking faults in the crystal structure.

temperature range, allowing only a partial phase transformation of the P-phase into the μ-phase.

An interesting observation in the present study is the presence of the μ-phase in the Ni–Cr–Mo–W alloys. The μ-phase has stoichiometry of the A_7B_6 type, and is commonly observed for binary systems Fe–W (Fe_7W_6), Fe–Mo (Fe_7Mo_6), Co–Mo (Co_7Mo_6) and Co–W (Co_7W_6). Although this is present in alloys of the type Ni–Cr–Mo, rhombohedral μ-phase types are not found in Ni–Cr, Cr–Mo and Ni–Mo binary systems. This indicates that the μ-phase in Ni alloys has actually a more complex composition with the element A consisting of Ni, Cr, Fe and Co, and the B element by refractory elements (Mo and W), as has been proven by chemical analysis, but always respecting the stoichiometry of the phase [30].

Tawancy [49] studied the formation of the μ–phase in various Ni-based alloys subjected to heat treatments between 540 °C to 870 °C for a period 1–16,000 h. The author mentions that the μ-phase is formed in compositions whose electron valence/atom (e/a) ratio is within the range 7.1–8.0. The explanation for the lack of a μ-phase for Ni_7Mo_6 or Ni_7W_6 type is precisely the value of the e/a ratio which is equal to 8.15. However, the author points out that the presence of small amounts of Fe and Co can assist in stabilizing the μ-phase by reducing the e/a ratio. Their results showed that among the alloys studied, the alloy C276 which has a Fe content of 5.5% was one that showed the highest levels of precipitation. For alloy Inconel 625 two compositions were tested, one with a Fe content of more than 3% and another with a Fe concentration of less than 3%. The analysis confirmed that only the alloy with the Fe content greater than 3% showed the formation of the μ–phase. Thus, the author suggests that a Fe concentration exceeding 3% may be sufficient to stabilize the μ-phase in Ni–Cr–Mo alloys.

As in the present study, all claddings had iron concentrations above 3 wt% due to dilution of the Ni alloy with the C–Mn steel substrate; therefore, there were favorable conditions for μ-phase stabilization. Thus, based on results of particles chemistry evaluated by EDS, the stoichiometric formula for the μ-phase of the precipitate can be written as $(Ni_{0.30}Cr_{0.19}Fe_{0.05})(Mo_{0.41}W_{0.7})$. The e/a ratio for the proposed expression was found to be 7.27, which is within the range indicated in the literature [49,50]. This chemical formulation is also in agreement with that reported by Raghavan et al. [48] for the μ-phase of the heat treated C276 alloy which is written as $(Ni_{0.36}Cr_{0.16}Fe_{0.04}Co_{0.02})(Mo_{0.39}W_{0.03})$.

However, the comments made by Tawancy [49] are based on the observation of a heat treated alloy and the precipitation of the μ–phase that occurs directly in the γ-fcc matrix or from M_6C and $M_{12}C$ carbides. For Ni–Cr–Mo weld metals, the microchemical composition is heterogeneous and the microstructure shows the presence of the P phase as a secondary reaction during the solidification or due to solid state transformation from the σ-phases. Thus the μ–phase becomes an evolution of the microstructure resulting from the partial transformation of P → μ. Considering the average composition of the P phase precipitated in the weld metal, the e/a ratio for the P phase was calculated as 7.39. This demonstrates that the P phase has a chemical composition whose e/a ratio is within the range favorable for μ–phase stabilization. Thus, the P phase concentration acts as a favorable site for the formation of the μ–phase. However, the μ–phase needs to change its stoichiometry and crystal structure, which is achieved by rejecting Cr and Ni from the P phase and this results in an enrichment of Mo and W.

Also some σ–phase precipitates, which have a tetragonal crystal structure with space group P4/mnm with lattice parameters: a = 0.88 nm; c = 0.454 nm were found in this work, especially in a higher dilution weld (sample C). Fig. 14a and b shows the TEM image in the bright field and dark field. Fig. 14a shows the selected area diffraction pattern of the oriented precipitate in the zone axis [115]. In the TEM bright field image the presence of defects in the crystal structure can be seen; these are probably stacking faults, similar to those observed in the μ–phase. Cieslak et al. [16] studied the microstructure of C22 and C276 alloys and showed that the σ–phases had stacking faults. Raghavan et al. [30] noted that the σ–phases found in the C276 alloy also showed stacking faults, however, in greater density than the P phase and in lower density than the μ–phase. These defects were highlighted in the TEM dark field image, obtained by the diffracted beam (411). The chemical composition of the σ–phase obtained by EDS analysis is shown in Fig. 14c. Based on the chemical analysis (Table 5) there were greater levels of Cr and Fe and lower levels of Ni and Mo if compared to the P and μ phases. The results are consistent with those observed for the σ–phase by Cieslak et al. [16] and Raghavan et al. [30].

The TEM results presented here clearly show the presence of three secondary phases in the γ–fcc matrix. In terms of the secondary phase the TCP phases found were: σ (tetragonal), P (Orthorhombic) and μ (rhombohedral).

3.3.3. X-ray electron diffraction analysis

In order to increase the volume of the analyzed material and to improve the identification of the phases formed in the weld metal,
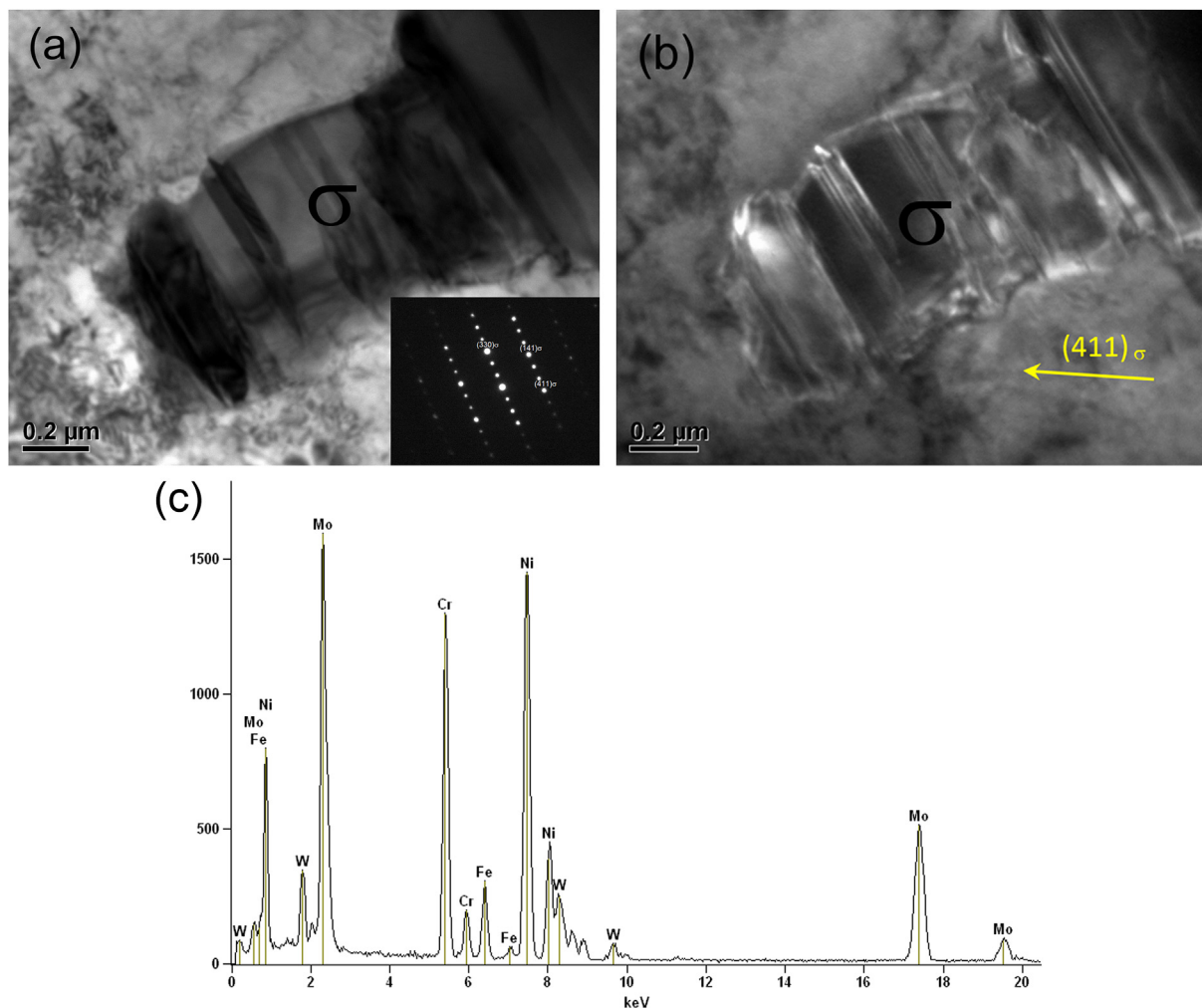
Fig. 14. TEM image of a σ-phase precipitated within the γ-matrix. (a) Bright-field image with selected area diffraction pattern oriented along [115] the axis zone; (b) Dark-field image; (c) Chemical analysis by EDS.

X-ray diffraction analyzes were performed on powder precipitates produced by the extraction technique in accordance with ASTM A923. The results of this analysis are shown in Fig. 15. Virtually all the peaks were indexed according to the standards of the P, μ and σ phases. However, in general, the results indicated that the secondary phases present in the alloy Inconel 686 are predominantly P, μ and σ phases in this order with the P phase being the most abundant. This result confirms the observations made by TEM, where the P phase was predominantly the main phase found.

In general, there is a lack of information on the metallurgical aspects of alloy Inconel 686. This alloy (Inconel 686) is derived from Hastelloy C276, with the same Mo and W content, but with the addition of Cr to give higher resistance to corrosion. Another alloy with a composition similar to alloy Inconel 686 is the C22 alloy. This alloy has a nominal Cr content (20 wt%), similar to alloy Inconel 686, however, it has almost 3% less Mo (nominal equal to 13 wt%).

The C22 alloy initially solidifies as a γ phase and at the end the liquid forms the P-phase [16,17,30], which is a different route compared to the C276 alloy. Cieslak et al. [16] suggested that the secondary phase formed at the end of solidification is a σ–phase, which subsequently becomes P phase by solid state transformation. Finally, the precipitation of the μ–phase occurs through the decomposition of the P phase, and the resultant microstructure is formed by γ + σ + P + μ. Perricone et al. [17] using thermodynamic

calculations suggested that both P phase and σ–phase are formed during solidification, and the P phase is the first to be formed.

Based on equilibrium thermodynamical calculation using Thermocalc the evolution of the microstructure for alloy Inconel 686 was determined. Fig. 16 shows that liquid is transformed to the fcc phase during solidification. After that the σ phase is formed, followed by transformation into the P phase. Although the results have been determined for equilibrium state conditions, which do not consider the heterogeneity of chemical composition due to segregation during the process of solidification, they indicate that both the σ and P phases can form in the alloy Inconel 686.

Pan et al. [51] also determined the evolution of the microstructure for alloy 22 by thermodynamic calculations (Fig. 17). The chemical composition of alloy 22 is somewhat similar to alloy Inconel 686, and has the same Cr content (20 wt%), a little less Mo (~2 wt% less), less than 1 wt% W and also the presence of 2–3 wt% Fe. Thus, the results for alloy 22 can also aid in the discussion of the solidification and phase transformation of alloy Inconel 686. It is possible to observe the initial P phase formation and its subsequent transformation into the μ–phase. Although the calculations of Pan et al. [51] indicate that there is an almost complete transformation of the phase P into μ, the short exposure time at high temperature suffered by the weld metal during thermal cycles of welding does not favor major changes of P phase into μ. This explains the
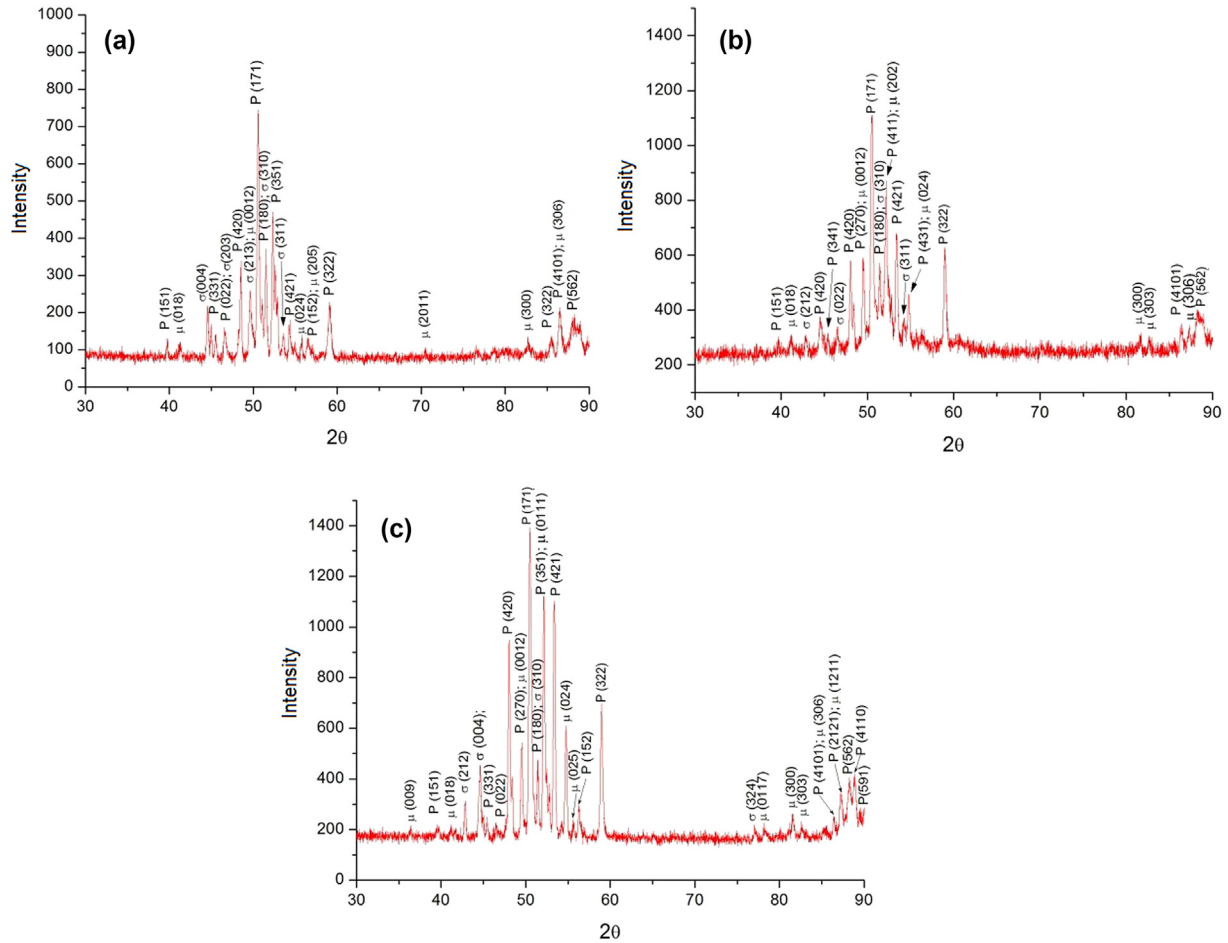
Fig. 15. X-ray diffraction spectrum of extracted precipitates from the bulk of the alloy Inconel 686. (a) Sample A; (b) Sample B (c) Sample C.
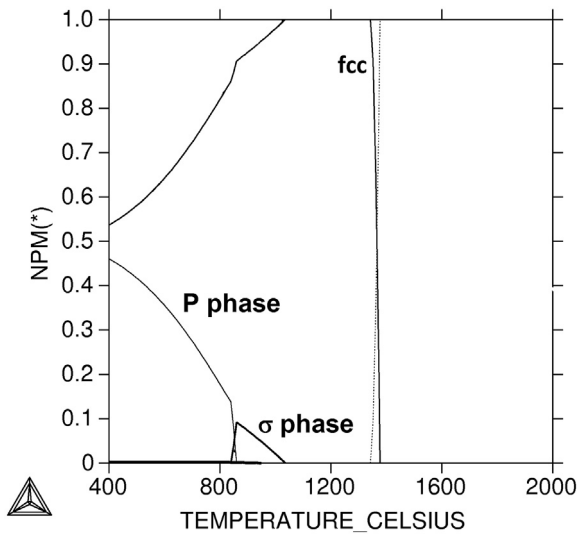

Fig. 16. Microstructural evolution × temperature diagram calculated based on the alloy Inconel 686 diluted weld metal evaluated in this study. (b) Calculated by Pan et al. for C22 alloy [51].

Fig. 17. Microstructural evolution × temperature diagram calculated by Pan et al. [51] for alloy C22.

predominance of P phase in the microstructure of alloy Inconel 686 compared to μ-phase.
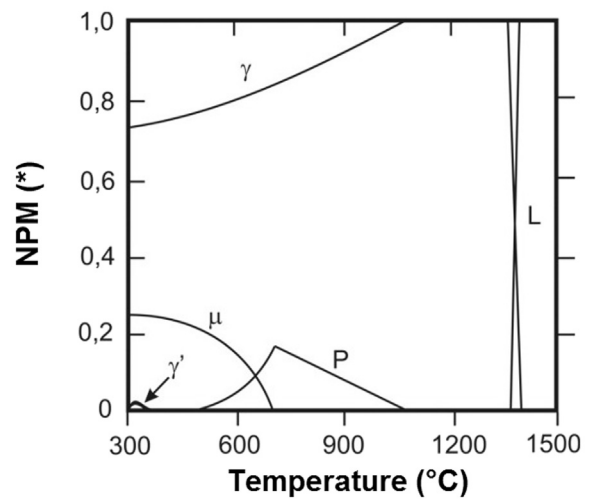
Based on the results presented in terms of distribution of elements in the matrix, and since the composition resembles the contents of alloying elements in the alloy 22 as well as the resultant microstructure, it is likely that the solidification path of the dissimilar weld metal resulted from the mixture of the alloy Inconel 686 and ASTM A516 Gr60 steel following a process similar to that

observed for the alloy 22. Initially, γ begins to solidify, rejecting some elements into the liquid metal, particularly Mo and W. Then the remaining liquid enriched with these elements between cells and/or secondary dendrite arms reaches favorable conditions for the solidification of the TCP phases, in this case, P and σ phases. At the end of solidification, due to the high temperature at which the material is, there is a transformation of the solid phase of $\sigma \rightarrow P$, and also the transformation of P into the μ-phase.

The presence of the σ phase in the microstructure can be attributed to at least two possibilities. The first is that from the incomplete solid-state transformation of σ−phase to the P phase occurs relatively quickly, which cannot fully transformation outside conditions of equilibrium. The other possibility is related to small fluctuations located within the chemical composition of the weld metal volume due to incomplete mixing of the melted metal, causing some areas to become slightly enriched in elements such as Fe and Cr, which are critical for the formation of the σ−phase. Thus, in these regions the solidification of the remaining liquid in the σ−phase is likely and this is maintained with cooling, preventing the transformation into the P phase. Regarding the solid state transformation it can be said that the P phase is partially transformed into the μ−phase.

4. Conclusions

Based on the results obtained and presented in this study on the microstructural characteristics of dissimilar weld overlays with alloy Inconel 686 deposited by the GTAW process with automatic cold wire feeding on C−Mn steel plates, it was concluded that:

✓ According to the microchemical analyses run by EDS, microsegregation occurred with Ni with k > 1, i.e. enriching the dendritic center while Mo segregated to liquid (k < 1). The results for Cr indicate a slight tendency to segregate to the liquid (k < 1), and the results for W were inconclusive as there were divergences from one sample to another;

✓ The results of the chemical composition of precipitates obtained by SEM and TEM indicated that the precipitates were constituted by Ni, Fe, Cr and were especially enriched with Mo and W.

✓ The topologically closed-packed TCP phases identified by TEM analysis according to selected areas electron diffraction patterns were P-phase, σ−phase and μ-phase.

✓ The X-ray diffraction analysis performed on powder of the precipitates extracted from the weld metal bulk identified P-phase, σ−phase and μ-phase confirming the results obtained by TEM.

Acknowledgements

References

[1] J.H. Perepezko, The hotter the engine, the better, Science 326 (Nov. 2009) 1068−1069.

[2] K. Lu, The future of metals, Science 328 (2010) 319−320.

[3] J.N. DuPont, Solidification of an alloy 625 weld overlay, Metall. Mater. Trans. A 27A (1996) 3612−3620.

[4] C.C. Silva, C.R.M. Afonso, A.J. Ramirez, M.F. Motta, H.C. Miranda, J.P. Farias, Metallurgical aspects of dissimilar weld overlays of Inconel 625 nickel based superalloys [In Portuguese], Sold. Insp. 17 (2012) 251−263.

[5] Q.H. Zhao, Y.P. Gau, J.H. Devletian, J.M. McCarthy, W.E. Wood, Microstructural analysis of Ni alloy 625 cladding over carbon steel, in: Proceedings of 3rd International Conference on Trends in Welding Research, ASM International, Materials Park, OH, 1993, pp. 339−343.

[6] F.G. Hodge, The history of solid-solution-strengthened Ni alloys for aqueous corrosion service, JOM 58 (9) (sep. 2006) 28−31.

[7] A.C. Lloyd, J.J. Noël, S. McIntyre, D.W. Shoesmith, Cr, Mo and W alloying additions in Ni and their effect on passivity, Electrochim. Acta 49 (2004) 3015−3027.

[8] S.J. Patel, A century of discoveries, inventors, and new nickel alloys, JOM 58 (9) (Sep. 2006) 18−20.

[9] J.N. Dupont, S.W. Banovic, A.R. Marder, Microstructural evolution and weldability of dissimilar welds between a super austenitic stainless steel and nickel-based alloys, Weld. J. 82 (6) (2003) 125−156.

[10] J.N. Dupont, C.V. Robino, J.R. Michael, M.R. Notis, A.R. Marder, Solidification of Nb-Bearing superalloys: part I. Reaction sequences, Metall. Mater. Trans. A 29A (Nov. 1998 a) 2785−2796.

[11] M.J. Cieslak, T.J. Headley, A.D. Romig, A melting and solidification study of alloy 625, Metall. Trans. A 19A (Set) (1988) p.2319−2331.

[12] C.C. Silva, C.R.M. Afonso, A.J. Ramirez, M.F. Motta, H.C. Miranda, J.P. Farias, New insight on the solidification path of an alloy 625 weld overlay, J. Mater. Res. Technol. 2 (3) (2013) 228−237.

[13] J.N. DuPont, C.V. Robino, J.R. Michael, M.R. Notis, A.R. Marder, Solidification of Nb-bearing superalloys: part I. Reaction sequences, Metall. Mater. Trans. A 29A (1998) 2785−2796.

[14] J.N. DuPont, C.V. Robino, A.R. Marder, M.R. Notis, Solidification of Nb-bearing superalloys: part II. Pseudoternary solidification surfaces, Metall. Mater. Trans. A 29A (1998) 2797−2806.

[15] S.W. Banovic, J.N. Dupont, A.R. Marder, Dilution and microsegregation in dissimilar metal welds between super austenitic stainless steel and nickel base alloys, Sci. Tech. Weld. Join. 7 (6) (2002) 374−383.

[16] M.J. Cieslak, T.J. Headley, A.D. Romig Jr., The welding metallurgy of HASTELLOY alloys C-4, C-22, and C-276, Metall. Trans. A. 17A (1986) 2035−2047.

[17] M.J. Perricone, J.N. Dupont, and M.J. Cieslak. Solidification of hastelloy alloys: an alternative interpretation. Metall. Mater. Trans. A. 34(5): 1127−1132.

[18] Q. Zhang, R. Tang, K. Yin, X. Luo, L. Zhang, Corrosion behavior of Hastelloy C-276 in supercritical water, Corros. Sci. 51 (2009) 2092−2097.

[19] M. Ahmad, J.I. Akhter, M. Akhtar, M. Iqbal, E. Ahmed, M.A. Choudhry, Microstructure and hardness studies of the electron beam welded zone of Hastelloy C-276, J. Alloy. Comp. 390 (2005) 88−93.

[20] P. Balu, P. Leggett, S. Hamid, R. Kovacevic, Multi-response optimization of laser-based powder deposition of multi-track single layer hastelloy C-276, Mater. Manuf. Proc. 28 (2) (2013) 173−182.

[21] C.C. Silva, E.C. de Miranda, M.F. Motta, H.C. de Miranda, J.P. Farias, Dilution control of weld overlay superalloys using Taguchi method, in: ASME 31st International Conference on Ocean, Offshore and Arctic Engineering, vol. 6, Rio de Janeiro, Brazil, July 1−6, 2012.

[22] C.C. Silva, C.R.M. Afonso, A.J. Ramirez, M.F. Motta, H.C. de Miranda, J.P. Farias, Evaluation of the corrosion resistant weld cladding deposited by the TIG cold wire feed process, Mater. Sci. Forum 783−786 (2014) 2822−2827.

[23] J.R. Hayes, J.J. Gray, A.W. Szmodis, C.A. Orme, Influence of chromium and molybdenum on the corrosion of nickel-based alloys, Corrosion 62 (6) (Jun. 2006) 491−500.

[24] SPECIAL METALS, INCONEL alloy 686-The alloy solution to fastener problems in the marine industry, Tech. Rep. (2005) 1−10.

[25] C. Thornton, C. Cooper, Overmatching superalloy consumable Inco-weld® 686CPT® broadens its applications to include welding super austenitic and superduplex stainless steels, in: Stainless Steel World 2004 Conference. Houston, Texas, USA, 2004. Paper No. SSW2005-P0468.

[26] INCONEL 686 Alloy, Special Metals Corporation, Publication Number SMC-024, 2005, p. 12.

[27] C.A. Maltin, A.M. Galloway, M. Mweemba, Microstructural evolution of Inconel 625 and Inconel 686CPT weld metal for clad carbon steel linepipe joints: a comparator study, Metall. Mater. Trans. A. 45A (July 2014) 3519−3532.

[28] R.B. Rebak, T.S. Edgecumbe Summers, R.M. Carranza, in: XXIII Scientific Basis for Nuclear Waste Management, Materials Research Society Symposium, 2000, p. 109. Warrendale, PA.

[29] B.S. El-Dasher, S.G. Torres, Second phase precipitation in as-welded and solution annealed alloy 22 welds, in: Pressure Vessel and Piping Conference, ASME International, Denver, CO, USA, 2005. Paper no. PVP 2005−71665.

[30] A. Raghavan, R.R. Mueller, G.A. Vaughn, S. Floreen, Determination of isothermal section of nickel rich portion of Ni-Cr-Mo system by analytical electron microscopy, Metall. Trans. A 15A (1984) 783−792.

[31] D.S. Dunn, Y.-M. Pan, L. Yang, G.A. Cragnolino, Localized corrosion susceptibility of alloy 22 in chloride solutions: Part 1 − mill annealed condition, Corrosion 61 (11) (Nov. 2005) 1078−1085.

[32] D.S. Dunn, Y.-M. Pan, L. Yang, G.A. Cragnolino, Localized corrosion susceptibility of alloy 22 in chloride solutions: Part 2 − effect of fabrication process, Corrosion 62 (1) (Jan. 2006) 3−12.

[33] J.N. Dupont, Microstructural development and solidification cracking susceptibility in the fusion zone of a stabilized stainless steel, Weld. J. 78 (7) (Jul. 1999) 253−263.

[34] M.F. Gittos, T.G. Gooch, Effect of iron dilution on corrosion resistance of Ni-Cr-

Mo alloy cladding, Br. Corros. J. 31 (4) (Apr. 1996) 309–314.

[35] M.J. Perricone, J.N. Dupont, Effect of composition on the solidification behavior of several Ni-Cr-Mo and Fe-Ni-Cr-Mo alloys, Metall. Mater. Trans. A. 37A (4) (Apr. 2006) 1267–1280.

[36] Z.F. Yin, W.Z. Zhao, W.Y. Lai, X.H. Zhao, Electrochemical behaviour of Ni-base alloys exposed under oil/gas field environments, Corros. Sci. 51 (2009) 1702–1706.

[37] C.C. Silva, E.C. Miranda, H.C. Miranda, M.F. Motta, J.P. Farias, A study about the contribution of the welding current and travel speed on the dilution and weld bead geometry deposited by GTAW process with cold wire feed, in: Proceeding, XXXVI CONSOLDA – National Welding Congress, Recife, Brazil, 2010 (In Portuguese).

[38] E.C. Miranda, C.C. Silva, H.C. Miranda, M.F. Motta, J.P. Farias, Influence of arc oscillation in dilution and geometric features of weld beads using GTAW cold wire feed process, Sold. Insp. 20 (2015) (2010) 180–190 (In Portuguese).

[39] S.W. Banovic, J.N. Dupont, A.R. Marder, Dilution control in gas-tungsten-arc welds involving superaustenitic stainless steels and nickel based alloys, Metall. Mater. Trans. B 32B (2001) 1171–1176.

[40] C.C. Silva, E.C. Miranda, M.F. Motta, H.C. Miranda, J.P. Farias, Influence of arc length on dilution and weld bead geometry of Ni-based alloy using GTAW process with cold wire feed, in: Proceedings, 20th International Congress of Mechanical Engineering, Brazilian Society of Mechanical Science and Engineering, Gramado, Brazil, 2009.

[41] E.C. Miranda, C.C. Silva, H.C. Miranda, M.F. Motta, J.P. Farias, Adjustment of the wire feeder parameters in GTAW process for coatings applications, in: Proceeding, XXXV CONSOLDA – National Welding Congress, Brazilian Welding Society, São Paulo, Brazil, 2009 (In Portuguese).

[42] M.J. Cieslak, T.J. Headley, G.A. Knorovsky, A.D. Romig Jr., T. Kollie, A comparison of the solidification behavior of INCOLOY 909 and INCONEL 718, Metall. Trans. A. 21A (1990) 479–488.

[43] A. Garner, Materials selection for bleached pulp washers, Pulp Pap. Can. 82 (1982) 109–120.

[44] S.D. Kiser, C. Cooper, Selection of nickel alloy welding products to provide maximum performance in severe pitting and crevice corrosion environments, in: Stainless Steel World Conference, the Hague, 1999. Paper No. SSW99–076.

[45] T.M. Pollock, The growth and elevated temperature stability of high refractory nickel-base single crystals, Mater. Sci. Eng. B 32 (3) (Jul. 1995) 255–266.

[46] J.D. Nystrom, T.M. Pollock, W.H. Murphy, A. Garg, Discontinuous cellular precipitation in a high-refractory nickel-base superalloy, Metall. Mater. Trans. A 28A (1997) 2443–2452.

[47] W.S. Walston, J.C. Schaeffer, W.H. Murphy, A new type of microstructural instability in superalloys, in: R.D. Kissinger, P.A. Warrendale (Eds.), Superalloys 1996, The Mineral, Metals and Metallurgical Society, 1996, pp. 9–18.

[48] M. Raghavan, B.J. Berkowitz, J.C. Scanlon, Electron microscopic analysis of heterogeneous precipitates in Hastelloy C-276, Metall. Trans. A. 13A (1982) 979–984.

[49] H.M. Tawancy, Precipitation characteristic of -phase in wrought nickel-base alloys and its effects on their properties, J. Mater. Sci. 31 (1996) 3929–3936.

[50] C.S. Barrett, T.B. Massalski, Structure of Metals, McGraw-Hill, New York, NY, 1966, p. 266.

[51] Y.-M. Pan, D.S. Dunn, G.A. Cragnolino, Topologically close-packed phase precipitation and thermal stability in alloy 22, Metall. Mater. Trans. A 36 (5) (May. 2005) 1143–1151.